Inorganic Chemistry Communications 152 (2023) 110729

Contents lists available at ScienceDirect

Inorganic Chemistry Communications

journal homepage: www.elsevier.com/locate/inoche

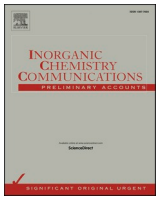

Short communication

Fabrication and studies of $LaFe_2O_3/Sb_2O_3$ heterojunction for enhanced degradation of Malachite green dye under visible light irradiation

Sabeeha Jabeen [a,b], Adil Shafi Ganie [c], Nafees Ahmad [a], Shariqah Hijazi [d], Shashi Bala [b], Daraksha Bano [e], Tahmeena Khan [a,*]

[a] Department of Chemistry, Integral University, Lucknow-226026, Uttar Pradesh, India
[b] Department of Chemistry, University of Lucknow, Lucknow-226007, Uttar Pradesh, India
[c] Department of Chemistry, Government Degree College, Banihal-182146, Jammu & Kashmir, India
[d] Organic Chemistry Section, Department of Chemistry, University of Kashmir, Hazratba-l 190006, Jammu & Kashmir, India
[e] Nano-Material Research Laboratory, Department of Chemistry, Indian Institute of Technology (BHU), Varanasi-221005, Uttar Pradesh, India

ARTICLE INFO

Keywords:
Photocatalyst
$LaFe_2O_3/Sb_2O_3$
Malachite green
Electrochemical double layer capacitance
Impedance
Nanocomposite

ABSTRACT

Visible light-driven photocatalysts with less charge transfer resistance and large separation are considered promising materials to address the challenges of environmental contamination. In this study, a nanocomposite of lanthanum ferrite and antimony oxide heterojunction ($LaFe_2O_3/Sb_2O_3$) was synthesized by facile hydrothermal method for photocatalytic degradation of malachite green (MG) dye under the irradiation of visible light. The synthesized nanocomposite was characterized by various analytical techniques including Fourier Transform Infrared Spectroscopy (FTIR) for functional group analysis, X-ray Diffraction (XRD) for phase purity and crystallinity, Scanning electron microscopy (SEM) for surface structure analysis, and energy dispersive spectroscopy (EDS) for surface composition. Moreover, the surface areas of the prepared samples were determined by the electrochemical double-layer capacitance (EDLC) using cyclic voltammetry. Impedance studies demonstrated lower charge transfer resistance for the heterojunction as compared to lanthanum ferrite and antimony oxide. The photocatalytic activity of the samples was checked for the decolorization of malachite green. It was observed that the nanocomposite showed maximum response with 98% degradation of MG in 88 minutes. Scavenging experiments established the involvement of hydroxyl radicals (OH) in the photodegradation mechanism of malachite green, while recycling experiments demonstrated its reliability and long-term use as a photocatalyst.

1. Introduction

Environmental contamination due to the rise in greenhouse gases, the release of recalcitrant pollutants, and rapid industrialization is a staggering problem of global concern. Environmental pollution is enlisted among the top ten prioritized issues of the world, which we are confronting in every facet of the biosphere [1,2]. Rapid industrialization has resulted in dumping a vast number of recalcitrant pollutants into the water bodies, thereby posing a serious threat to the quality and composition of these water bodies. Various pollutants such as textile dyes, phenols, volatile organic compounds, pesticides, fungicides, and phthalates have been added to the environmental media and have deteriorated their quality and standard [3–5]. In addition to pollutants, the addition of several endocrine disruptors, such as 17-β-estradiol, polybrominated biphenyls (BBPs), polychlorinated biphenyls (PCBs), and bisphenol A (BPA) in the environment has resulted in serious health problems [6–8]. Researchers across the globe are devoting their persistent efforts to developing effective technologies to remediate and mitigate the harmful effects of these contaminants. To date, several techniques have been developed like adsorption method, coagulation, flocculation, microfiltration, and precipitation [9,10]. But due to their time-consuming nature, they face several drawbacks in the complete degradation of pollutants. Photocatalysis using metal oxide nanomaterials is considered a sustainable technique to degrade organic and inorganic pollutants [11–13]. Although, photocatalysis is considered a signature technology for degrading pollutants, but its application is limited because of the photocatalysts possessing wide band gaps.

Metal oxide nanostructures are being increasingly researched and receiving considerable attention in photocatalytic and electrocatalytic activities, because of their functional morphologies and peculiar

* Corresponding author.
E-mail address: tahminakhan30@yahoo.com (T. Khan).

https://doi.org/10.1016/j.inoche.2023.110729
Received 18 December 2022; Received in revised form 4 April 2023; Accepted 16 April 2023
Available online 26 April 2023

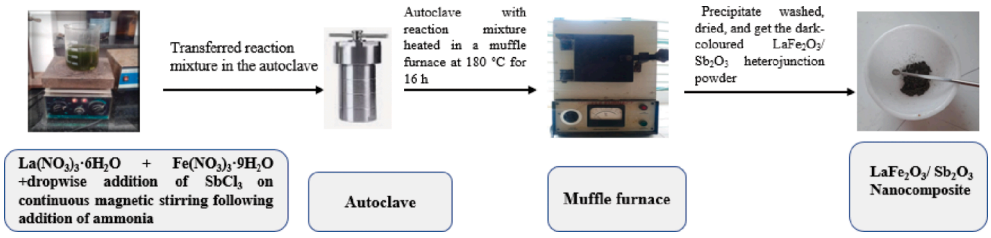

Fig. 1. Synthetic Route for $LaFe_2O_3/Sb_2O_3$ (LaSb) nanocomposite.

properties [14,15]. The peculiar features of metal oxide-based photocatalysts are remarkably utilized for the reclamation and remediation of contaminated environments. However, these metal oxide nanostructures suffer serious drawbacks in light absorption and surface redox properties, limiting their activities [16]. To overcome that, two different metal oxides have been coupled to form a binary metal oxide, which can improve the absorption as well as redox properties of the system. Amongst all binary metal oxide nanostructures, perovskite oxides having a composition of ABO_3 are the most significant functional materials due to their rich physical properties such as dielectric, ferromagnetism, multiferroic properties, etc. Recent curiosity in nano techniques and nanostructured materials has led to prodigious efforts directed at the fabrication of low-dimensional perovskite oxide-based nanostructured materials to improve and understand their innovative characteristics at the nanoscale [17]. Usually, in the ABO_3 perovskite structure, A-site is engaged by alkaline earth metals or rare-earth metals, and B-site is engaged by transition metal ions. Different rare earth perovskite manganites have been explored to demonstrate a strong coupling between their magnetic and structural order parameters. For example, a magnetically induced structural phase transition has been observed in $La_{0.83}Sr_{0.17}MnO_3$, indicating strong coupling between the local magnetic spin moments and the lattice structure. Furthermore, low-dimensional perovskite oxides nanostructures such as nanowires, nanorods, nanotubes, and nanofibers, show a significant character in developing the next generation of metal oxide-based nanostructures. In the past few years, much effort has been made in the synthesis of perovskite oxide nanostructures by various methodologies. The functional applications of perovskite oxide nanostructures are also explored in the fields of wastewater remediation, energy harvesting, and solar energy conversion [18,19].

Metal oxide-based materials have also shown excellent applications in degradation processes due to large specific surface area, excellent redox properties, good thermal stability, and fast electron transfer. Various metal oxide and their composites have been utilized as photocatalysts like $LaFeO_3$/g-C_3N_4, NiO, CuO, Ag_2S@NiO-ZnO, etc. Metal oxide nanostructures have recently emerged as promising materials for a variety of applications, including electrochemical trace pollutant detection, photodegradation of textile dyes, immunosensing, tissue engineering, energy storage, catalysis, and food packaging [20–23]. Among various metal oxide nanostructures, lanthanum-based nanostructures have shown good catalytic properties, because of their high thermal stability, electrical conductivity, and tunable properties [24–26]. Although they are prone to oxidation, yet they have shown excellent redox behavior, efficient catalytic activity, and increased specific surface area. Moreover, these photocatalysts have shown low band gaps and increased light absorption, which has made them potential catalysts for photodegradation processes [27,28].

In the present study, we report the synthesis of lanthanum ferrite and antimony oxide by sol–gel and hydrothermal methods, respectively. Then the synthesis of binary $LaFe_2O_3/Sb_2O_3$ heterojunction nanocomposite was done by hydrothermal method The synthesized nanostructures were used as photocatalysts for the degradation of textile dye, Malachite green which is a triphenylmethane dye generally used as a fungicide, in paper coluring productions and also used in fabric manufacturing industries. It is a cationic water-soluble dye that is a probable cause of carcinogenesis, mutagenesis, chromosomal disorders, and blockage of respiratory tract [29]. In the present work, the degradation of malachite green dye under visible light irradiation was carried out using $LaFe_2O_3/Sb_2O_3$ heterojunction nanocomposite as a catalyst. The fabrication of binary metal oxide nanocomposite has an advantage over individual counterparts in light absorption, redox activity, and interfacial charge transfer.

2. Experimental section

2.1. Materials and chemicals

All chemicals used in the study were of analytical grade and free from impurities. Ferric nitrate ($Fe(NO_3)_3·9H_2O$), Lanthanum Nitrate, ($La(NO_3)_3·6H_2O$), antimony trichloride ($SbCl_3$), and ammonia solution were purchased from Sigma Aldrich. Malachite green, Isopropyl alcohol, benzoquinone, and sodium nitrate were purchased from Alfa Aesar.

2.2. Synthesis of Lanthanum Ferrite ($LaFe_2O_3$) nanostructure

Lanthanum Ferrite was synthesized by sol–gel method using citric acid as a complexing agent [30]. The procedure involved the dissolution of 5 mmol each of $La(NO_3)_3·6H_2O$ and $Fe(NO_3)_3·9H_2O$ in 30 mL of deionized (DI) water . After that, 10 mmol of citric acid was added, and the mixture was magnetically stirred for 18 h at 80 °C. The gel obtained after stirring was dried in an oven at 80 °C until an amorphous sample was obtained. The amorphous mass was first calcined at 400 °C for 4 h and then at 650 °C for 3 h. The compound was then cooled at room temperature, and crushed in mortar and pestle to get a finely powdered sample.

2.3. Synthesis of antimony oxide (Sb_2O_3) nanostructure

Antimony oxide was synthesized by hydrothermal method [23]. The procedure involved the dissolution of 0.05 mol of antimony trichloride ($SbCl_3$) in 50 mL of deionized water at room temperature. Under continuous stirring, the formation of a white insoluble precipitate took place. After that, the pH was maintained at 10 with the addition of an appropriate amount of ammonia ($NH_3·H_2O$) solution. The mixture was vigorously stirred for about 30 min and then transferred into an 80 mL Teflon-lined stainless autoclave. The autoclave was sealed and maintained at 120–180 °C for 10 h. After the reaction was complete, the resulting white solid product was filtered and washed with water and absolute alcohol several times. After drying in a vacuum at 60 °C for 3 h, the white powder was obtained.

2.4. Synthesis of $LaFe_2O_3$/ Sb_2O_3 heterojunction nanocomposite

The synthesis of $LaFe_2O_3$/ Sb_2O_3 heterojunction nanocomposite was done by hydrothermal method. In a typical procedure, 2.0 mmol each of $La(NO_3)_3·6H_2O$ and $Fe(NO_3)_3·9H_2O$ were dissolved in 60 mL of deionized water. To this solution, 5 mmol of $SbCl_3$ was added on continuous magnetic stirring. After that, an appropriate amount of ammonia

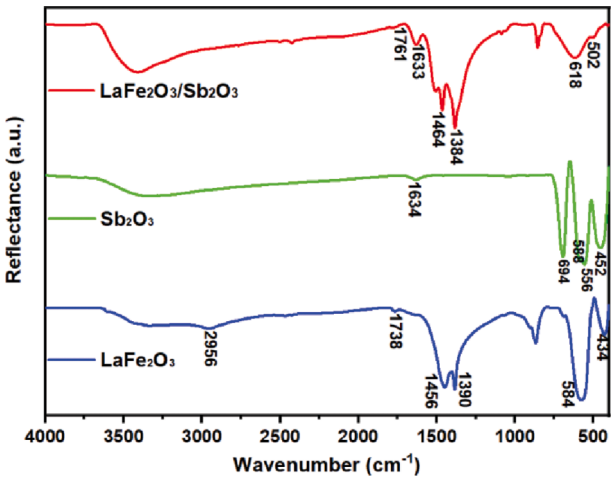

Fig. 2. FTIR spectra of $LaFe_2O_3$, Sb_2O_3 and $LaFe_2O_3$ /Sb_2O_3 (LaSb) nanostructured materials.

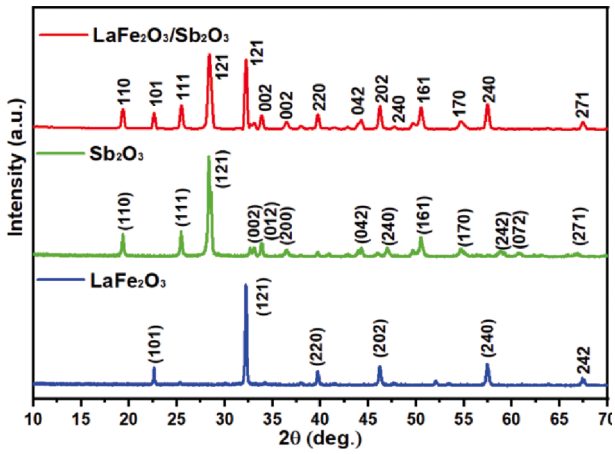

Fig. 3. XRD spectra of $LaFe_2O_3$, Sb_2O_3 and $LaFe_2O_3/Sb_2O_3$ (LaSb) nanostructured materials.

solution was added and the mixture was magnetically stirred for 6 h. After vigorous stirring, the mixture was transferred into a Teflon-line stainless autoclave and heated at 180 °C for 16 h. The resulting precipitate was filtered, washed several times with DI water followed by ethanol, and then dried at 80 °C to get the dark-colored $LaFe_2O_3/Sb_2O_3$ heterojunction powder. Fig. 1**,** depicts the fabrication route of $LaFe_2O_3$/Sb_2O_3 (LaSb) Nanocomposite.

2.5. Material characterizations

The functional group analysis was carried out by Perkin Elmer spectrum-2 Fourier Transform Infrared Spectrometer. Phase purity, lattice size, and morphology of the nanostructures were evaluated by Schimadzu-6100 X-ray diffractometer of 40 Kv tube voltage and Cu Kα radiations of wavelength 1.5418 Å. The optical studies and band gap analysis were done with a Perkin Elmer UV–vis NIR spectrometer. Surface structure and elemental composition were investigated by scanning electron microscope (JSM 6510 LV JEOL Japan) fitted with a 15 KeV energy dispersive X-ray detector (EDS). Topography and selected area diffraction was studied by Transmission electron microscope (JOEL-JSM 6360, Japan).

2.6. Cyclic voltammetry

Cyclic voltammetry was performed using three electrode system PGSTAT204-Autolab instrument, with Ag/AgCl as the reference electrode, glassy carbon as the working electrode, and platinum rod as the counter electrode. All voltammetric experiments were carried out in 0.1 M Phosphate buffer at room temperature. Electrochemical Impedance studies were carried out at an open potential of 10 mV using 1.0 mM $K_3[Fe(CN)_6]$ in 0.1 M KOH as a redox probe.

2.7. Photocatalytic test procedure

The photocatalytic reaction was performed in a Pyrex glass jacketed photoreactor with outer and inner chambers with continuous water circulation to maintain temperature. The irradiating lamp (halogen lamp, 500 W, 9500 lm) was placed in the inner chamber and the dye solution was fed into the outer chamber having an opening for molecular oxygen. The Malachite green dye solution and the appropriate amount of catalyst (1 mM with 1 mg L^{-1}) were magnetically stirred for 30 min before irradiation.

The photoreaction occurred in the outer chamber after the irradiating lamp was turned on and the dye aliquots were taken after regular intervals of time. These aliquots were centrifuged and then analyzed in a UV–vis spectrophotometer to measure maximum absorbance. From the absorbance values, the degradation efficiency was deduced by Eq. (1).

$$\text{Degradation efficiency} = C_0 - C_t/C_0{*}100 \quad (1)$$

where C_0 is the initial concentration of dye and C_t is the concentration after the time (t).

3. Results and discussion

3.1. Fourier Transform Infrared spectroscopy (FTIR) analysis

FTIR was carried out to study the functional groups present in the synthesized nanomaterials. The FTIR spectra of $LaFe_2O_3$, Sb_2O_3, and $LaFe_2O_3/Sb_2O_3$ are shown in Fig. 2. The peaks around 3200–3400 cm^{-1} corresponded to the O—H stretching vibrations of physisorbed water on the surface. The peaks around 400–600 cm^{-1} were attributed to M—O and O—M—O peaks (M = La, Sb, Fe, etc.) [31]. In the spectrum of $LaFeO_3$, The peaks at 434 cm^{-1} and 584 cm^{-1} were credited to the vibrations of the Fe—O bond and La—O, The complexation process between citric acid and metal ions was established by transmission bands at 1456 cm^{-1}. Peak obtained at 2956 cm^{-1} was attributed to the C—H stretching. Bands allocated at 1738, 1356 cm^{-1} were ascribed to the C═O, H—O—H/carboxylate, bending vibrations of the water molecules and nitrate groups respectively [32]. In the case of Sb_2O_3 the absorption bands at 452 cm^{-1}, 556 cm^{-1}, 588 cm^{-1}, and 694 cm^{-1} were attributed to the stretching frequencies of Sb—O, oxide bridge functional group (O—Sb—O) and symmetric and asymmetric vibration of Sb_2O_3 [33].

3.2. X-Ray Diffraction (XRD) analysis

The phase purity, crystallinity, and surface composition were analyzed by X-ray diffraction (XRD) analysis. The XRD spectra of $LaFe_2O_3$, Sb_2O_3, and $LaFe_2O_3/Sb_2O_3$ Nanostructure materials are depicted in (Fig. 3**).** In $LaFe_2O_3$, the peaks were centered at 22.51°, 32.12°, 39.56°, 46.15°, 57.32°, and 67.42° corresponding to 2θ values of (101), (121), (220), (202), (240), and (242) and matched well with the JCPDS file PDF 00-037-1493 [34]. While in the case of orthorhombic Sb_2O_3, the peaks were well consistent with JCPDS card No. 11-0689 [35]. The peaks corresponded to 2θ values of 19.36°, 25.44°, 28.38°, 31.98°, 32.9°, 33.86°, 36.52°, 44.36°, 47.04°, 50.48°, 54.72°, 59.12°, 60.98°, and 66.9° which corresponded to (110), (111), (121), (131), (002), (012), (200), (042), (240), (161), (170), (242), (072), and (271) planes. The average crystallite size of the prepared nanostructures and the corresponding nanocomposite were elucidated by using the Debye-Scherer formula (Eq. (2)) using the full width at half maximum

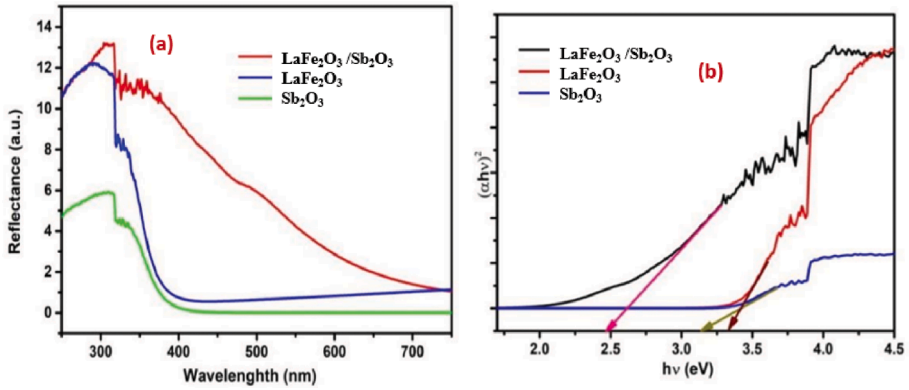

Fig. 4. (a) UV-DRS spectra and (b) Tauc's plots of $LaFe_2O_3$, Sb_2O_3, and $LaFe_2O_3$ /Sb_2O_3 (LaSb) nanostructured materials.

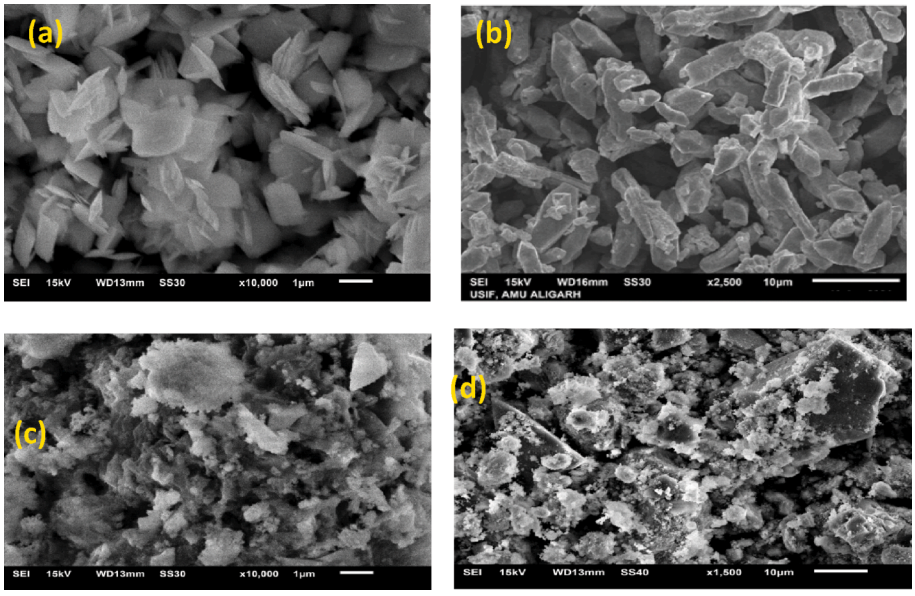

Fig. 5. SEM micrographs of (a) Sb_2O_3, (b) $LaFe_2O_3$, (c and d) $LaFe_2O_3$/Sb_2O_3 nanostructured materials at different resolution.

(FWHM) value of the main intense peak.

$$D = \frac{k\lambda}{\beta Cos\theta} \tag{2}$$

where 'D' is the average crystallite size of the nanostructures, β is the FWHM value of the most intense peak, λ is the wavelength k is constant and θ is Braggs angle. From Eq. (2), the average crystallite size of Sb_2O_3, $LaFe_2O_3$, and $LaFe_2O_3$ /Sb_2O_3 nanostructured materials was calculated to be 33 nm, 54 nm, and 21 nm respectively which is in line with the previous literature [34,36].

3.3. Optical properties

The optical properties were studied by Ultra-Violet diffuse reflectance (UV-DRS) spectroscopy. The DRS spectra of $LaFe_2O_3$, Sb_2O_3, and $LaFe_2O_3$ /Sb_2O_3 nanostructures are shown in Fig. 4a. The optical absorbance of $LaFe_2O_3$ and Sb_2O_3 nanostructured materials lied around 350 nm in the UV region while the optical absorbance of $LaFe_2O_3$/Sb_2O_3 nanocomposite lied around 420 nm in the visible region. The shift in the absorption towards the longer wavelength (red shift) can be due to the formation of the interface at the junction of two different nanoparticles which resulted in increased absorption in the visible region.

The optical band gaps were calculated from Tauc's plots using Eq. (3):

$$h\nu.\alpha = \left(Ah\nu - E_g\right)^{n/2} \tag{3}$$

The above equation can be transformed to Kulbeka-Munk function form in Eq. (4):

$$h\nu.F(R) = \left(Ah\nu - E_g\right)^{n/2} \tag{4}$$

where Eg is the optical band gap, F(R) is the K-M function, ν is the frequency of light and A is a constant. From the plot of $(F(R) \times h\nu)^{1/2}$ versus hν (Fig. 4b), the optical band gaps of $LaFe_2O_3$, Sb_2O_3, and $LaFe_2O_3$/Sb_2O_3 Nanostructured materials were calculated to be 3.3 eV, 3.2 eV, and 2.4 eV, respectively. The lower band gap of the composite $LaFe_2O_3$/Sb_2O_3 can be attributed to the better absorption in the visible region which may increase its catalytic activity in the visible region.

3.4. Morphological and topographical studies

The surface morphology, topography, and surface composition of the prepared composites can be studied by electron microscopy. The typical SEM micrographs of $LaFe_2O_3$, Sb_2O_3, and $LaFe_2O_3$/Sb_2O_3 nanostructures are shown in Fig. 5a-d. As seen in Fig. 5a, the Sb_2O_3, nanostructures exhibited rough sphere-shaped morphology with porous nature which is related to the catalytic activity. While the $LaFe_2O_3$, nanostructure possessed rod-shaped morphology (Fig. 5b) with little

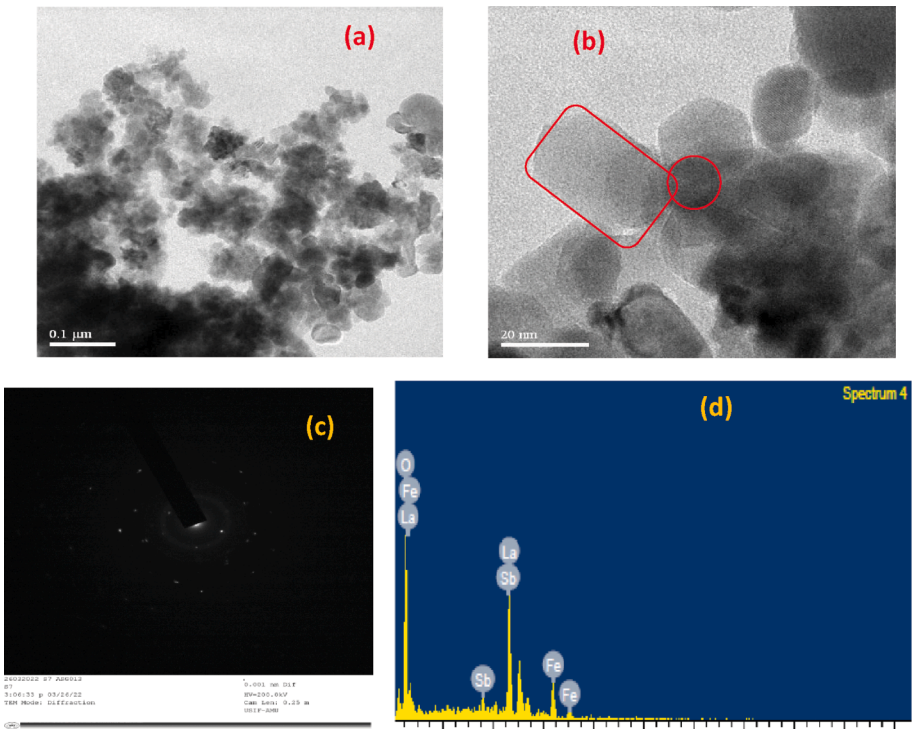

Fig. 6. (a and b) TEM micrographs of $LaFe_2O_3/Sb_2O_3$nanocomposite at different magnifications, (c) SAED pattern of $LaFe_2O_3$ /Sb_2O_3 nanocomposite (d) EDS spectra of $LaFe_2O_3/Sb_2O_3$ nanocomposite.

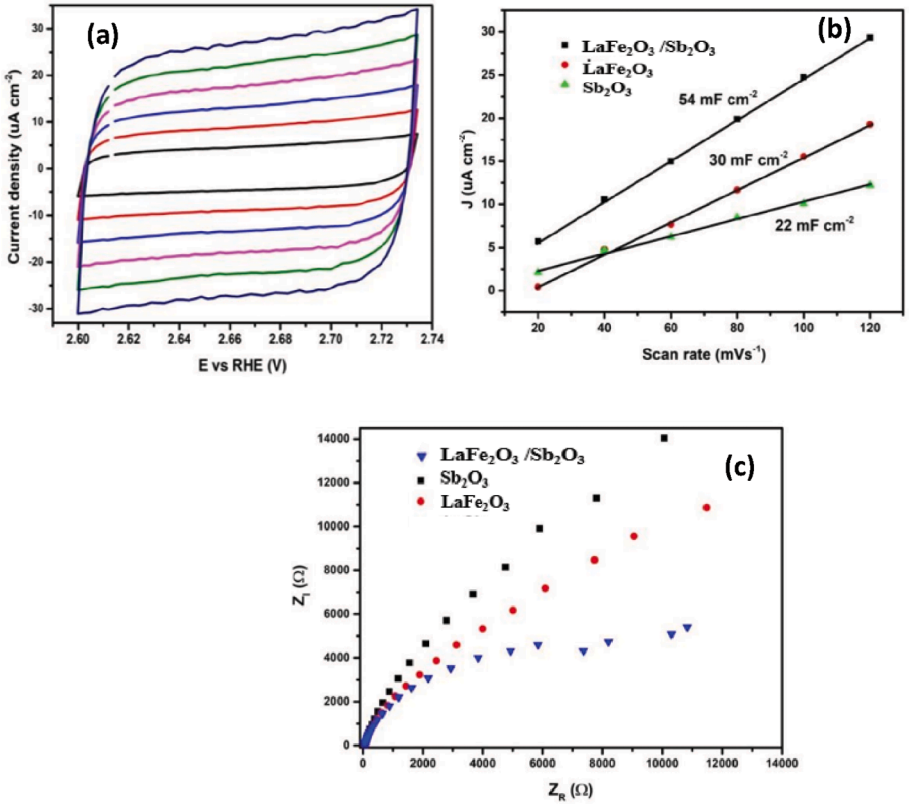

Fig. 7. (a) Cyclic voltammograms of $LaFe_2O_3/Sb_2O_3$ at different scan rates. (b) Capacitive current as a function of scan rate for $LaFe_2O_3$, Sb_20_3, and $LaFe_2O_3/Sb_2O_3$ nanocomposite. (c) Nyquist plots or EIS spectra of different catalysts.

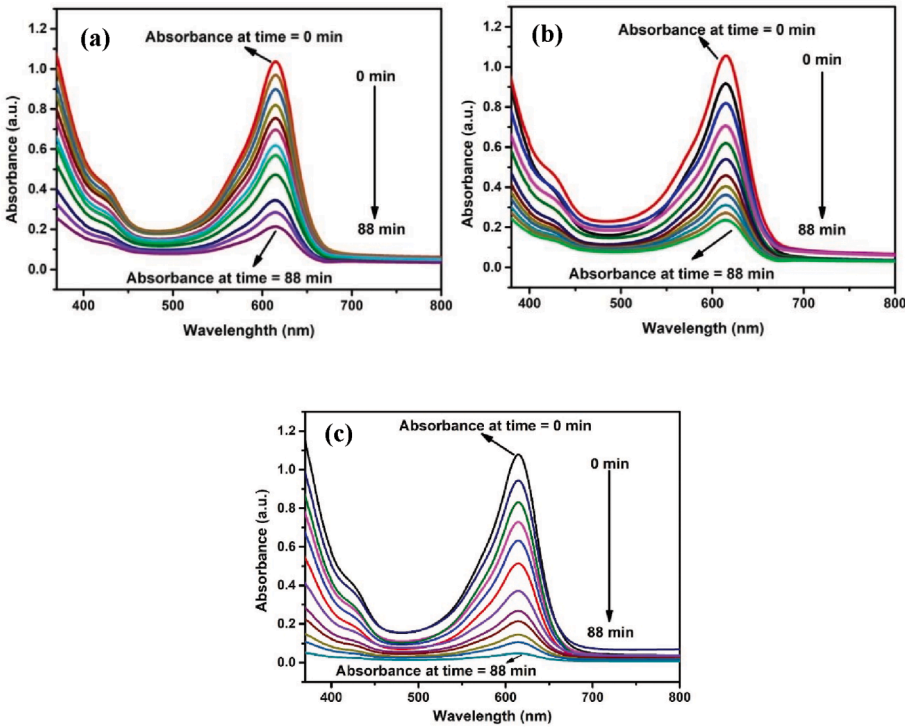

Fig. 8. UV–Visible absorption spectra of Malachite Green in presence of (a) $LaFe_2O_3$, (b) Sb_2O_3 and (c) $LaFe_2O_3/Sb_2O_3$ nanostructured materials under visible light irradiation. (For interpretation of the references to colour in this figure legend, the reader is referred to the web version of this article.)

agglomeration. The composite had irregular morphology with the Sb_2O_3 nanostructure being adhered to the surface of the $LaFe_2O_3$ nanostructure (Fig. 5c). The overall morphology of the nanocomposite depicted the random distribution of Sb_2O_3 nanostructures over $LaFe_2O_3$, nanostructures which have led to increased reactive sites and probably may have resulted in an increased surface area.

Further insight into the morphological structure of composite can be gained from Transmission electron microscopy (TEM). Fig. 6a-b depict the TEM images of $LaFe_2O_3/Sb_2O_3$ nanocomposite at two different resolution powers. The TEM images clearly showed the heterojunction formation between the Sb_2O_3 nanostructure and $LaFe_2O_3$ nanostructure, the particles were irregularly distributed on one another with different morphologies particularly the spherical morphology of Sb_2O_3 and perovskite morphology of $LaFe_2O_3$ nanostructure. SAED patterns (Fig. 6c) depicted bright spots with concentric diffraction rings which can be assigned to different crystal planes in a composite, suggesting a polycrystalline behavior of the nanocomposite with crystal planes of different nanostructured materials. Surface composition was determined by energy dispersive spectroscopy (EDS) and from the EDS spectra of $LaFe_2O_3$ /Sb_2O_3 nanocomposite, lanthanum, antimony, iron, and oxygen were detected, as shown in Fig. 6d. The absence of any other element demonstrated that no impurity was present in the synthesized nanocomposite and no contamination occurred during the composite formation.

3.5. Effective surface area measurement

The active surface areas of the prepared samples were determined by the electrochemical double-layer capacitance (EDLC), by performing cyclic voltammetry in a non-faradic range at different scan rates [37,38]. The cyclic voltammograms at different scan rates (20–100 $mVsec^{-1}$) are shown in Fig. 7a. The electroactive surface area was calculated from the slope of scan rate vs capacitive current (Fig. 7b), which was approximately equivalent to twice the double-layer capacitance (C_{dl}). From the slope, the electroactive surface area of Sb_2O_3, $LaFe_2O_3$, and $LaFe_2O_3/Sb_2O_3$ nanostructured materials were calculated to be 22 mF cm^{-2}, 30 mF $cm^{-2,}$ and 54 mF cm^{-2} respectively. The increase in the surface area of composite nanomaterial can be attributed to the effective heterojunction formation which may lead to an increase in surface active sites and enhanced catalytic activity.

3.6. Electrochemical Impedance studies

Electrochemical impedance studies are performed to investigate the electrode kinetics and interfacial interactions across the interfaces of electrode reactions [39,40]. The EIS plots, also called as Nyquist plots are used for determining the charge transfer resistances across the interfaces. The EIS plots of $LaFe_2O_3$, Sb_2O_3, and $LaFe_2O_3/Sb_2O_3$ nanostructured materials are depicted in Fig. 7c. From the spectra, it can be seen that the A_{ct} of Sb_2O_3 nanostructured material had maximum valu, followed by $LaFe_2O_3$ nanostructured material and $LaFe_2O_3/Sb_2O_3$ nanocomposite. The lowest value was seen for $LaFe_2O_3/Sb_2O_3$ nanocomposite which can be due to fast electron transfer across the interface. The formation of binary nanocomposite may have facilitated efficient electron transfer and resulted in lower impedance which can prove beneficial for the catalytic activity of composite.

3.7. Evaluation of photocatalytic degradation of dye and mechanistic approach

The photocatalytic activity of the prepared nanostructured materials was investigated for degradation and decolorization of malachite green in aqueous media under visible light illumination. For the comparative study of the photodegradation of the selected dye, the same amount of each sample was utilized. A dye solution with an initial concentration of C_0 was prepared, and 0.3 mg of $LaFe_2O_3$, Sb_2O_3, and $LaFe_2O_3/Sb_2O_3$ nanostructured materials were added to it in separate beakers. Before irradiation, the samples were agitated for 20 min in dark to check the adsorption/desorption equilibrium. In all the settings in dark, the dye concentration does not change, suggesting very little or insignificant adsorption. Then, the reaction chamber was irradiated with visible light to form photoexcited charge carriers (electron (e^-) and hole (h^+), with a

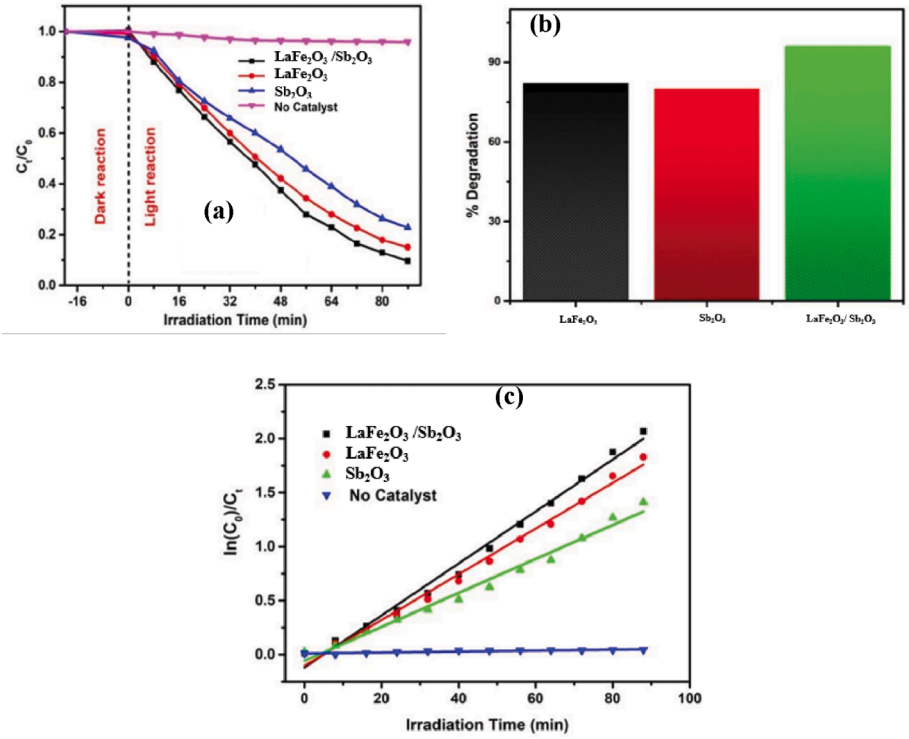

Fig. 9. (a) Residual concentration of Malachite green with time in different reaction settings and presence of $LaFe_2O_3$, Sb_2O_3, and $LaFe_2O_3/Sb_2O_3$ nanocomposite. (b) Bar chart showing degradation percentage of MG over $LaFe_2O_3$, Sb_2O_3 and $LaFe_2O_3/Sb_2O_3$ nanocomposite (c) First order rate kinetics of photodegradation reactions. (For interpretation of the references to colour in this figure legend, the reader is referred to the web version of this article.)

Table 1
Comparative study of the % degradation of Malachite green by various nanocomposite.

Catalyst system	Degradation (%)	Time duration	Light used	Catalysts dosage	Literature
Fe doped TiO_2	81	30 h	Visible	19 mg/mL	[47]
Zn-Mn	93	2 h	UV	25 ppm	[48]
$ZnVFeO_4$	90.1	2.5 h	Visible	1.0 g/L	[49]
ZnO/CNT	79	1 h	Visible	0.1 g/L	[50]
Chitosan/ Ce-ZnO	80	1 h	Visible	0.2 g/L	[51]
$LaFe_2O_3$/ Sb_2O_3	98	88 min	Visible	1 mg/mL	Present study

125 W medium pressure mercury lamp (Philips) with an intensity of UV–visible light ranging from 1.92 to 1.98 m W/cm^2 [41]. After irradiation, aliquots at regular intervals were taken from the reaction mixture and their corresponding concentration was determined by Beer-Lamberts law using a UV visible spectrophotometer after centrifugation. The UV–vis spectra of $LaFe_2O_3$, Sb_2O_3, and $LaFe_2O_3/Sb_2O_3$ nanostructured materials are depicted in Fig. 8a–c. The comparative activity of the catalysts was examined and is depicted in Fig. 9a. It is evident from Fig. 9a, that without the addition of the catalysts; the concentration of the dye almost remained the same after 88 min, suggesting the importance of photocatalysts in the photodegradation reaction. It is also clear , that the degradation efficiency increased on forming heterojunction between $LaFe_2O_3$ and Sb_2O_3. The degradation efficiency of Sb_2O_3, $LaFe_2O_3$, and $LaFe_2O_3/Sb_2O_3$ nanostructured material was found to be 80%, 82%, and 98% respectively (Fig. 9b). The increase in photocatalytic activity can be due to an increase in reactive site, charge transfer across the interfaces, and efficient absorption of visible light. The increase in photocatalytic activity is well supported by a decrease in charge transfer resistance in EIS studies and an increase in surface area as shown in EDLC studies. The primary variables affecting dye degradation are electrostatic interactions between anionic dye and the cationic surface of the nanocatalyst, large surface area, and the presence of reactive functionalities present on the surface of $LaFe_2O_3/Sb_2O_3$ nanocomposites. The results were compared with already reported literature and it was found that the $LaFe_2O_3/Sb_2O_3$ nanocomposites as photocatalysts were much more efficient in both activity and execution. The comparative results have been depicted in Table 1.

The kinetics of photodegradation were also studied using the Langmuir-Hinshelwood first-order model (Eq. (5)) [42]:

$$ln\left[\frac{C_0}{C_t}\right] = K_{app}t \tag{5}$$

where C_0 and C_t represent the dye concentrations at the time '0′ and 't' respectively, and 'K_{app}' represents the apparent pseudo-first-order rate constant. The rate constants calculated for $LaFe_2O_3$, Sb_2O_3 and $LaFe_2O_3/Sb_2O_3$ nanostructured materials were 0.00399 min^{-1}, 0.00359 min^{-1}, and 0.00523 min^{-1} respectively. The kinetics of photodegradation is represented in Fig. 9c.

3.7.1. Mechanism of photodegradation

The valence and conduction band edge potentials of the pure nanocatalysts were used to investigate the photocatalytic mechanism, The E_{VB} can be estimated using the following Eq. (6) [43]:

$$E_{VB} = X - E^e + 0.5E_g \tag{6}$$

where X denotes the electronegativity of the constituent atoms, E_g denotes the band gap energy, and E^e denotes the energy of free electrons (i.e. 4.5 eV).

Whereas the catalyst's E_{CB} was determined using Eq. (7) [44]:

$$E_{CB} = E_{VB} - E_g \tag{7}$$

When a photon with hν energy from a visible light source collides with the surface of NPs, an electron (e^-) in the valence band (VB)

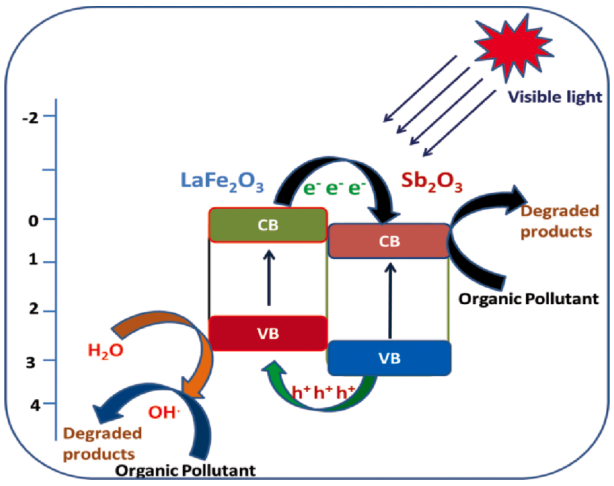

Fig. 10. Plausible Mechanism of Malachite green dye degradation on $LaFe_2O_3$/Sb_2O_3 nanocomposite heterojunction. (For interpretation of the references to colour in this figure legend, the reader is referred to the web version of this article.)

becomes excited and jumps to the conduction band (CB), leaving a hole (h^+) in the valence band. Holes react with the hydroxyl groups of water (H_2O) to produce hydroxyl radicals ($OH^\bullet$) in a very short time. The redox potential of $^-OH/^\cdot OH$ and O_2/O_2^- is 2.38 V and −0.33 V (vs NHE) respectively [45,46]. The valence band potential of $LaFe_2O_3$ was calculated to be 2.43 V, which is more positive than the redox potential of $^-OH/^\cdot OH$ and is sufficient to oxidize OH^- to $^\cdot OH$ radical. However, the conduction band potential of $LaFe_2O_3$ was calculated to be −0.02 eV and that of Sb_2O_5 is 0.03 eV, which was much more positive than the redox potential of O_2/O_2^-, therefore, there is the least chance for the generation of O_2^- radical, but the CB potential was sufficient for the formation of peroxide radical (O_2/H_2O_2, 0.685 eV vs NHE), which in turn can generate $^\cdot OH$. These radicals may act upon the photocatalyst and degrade them.

The electrons accumulated in the conduction band then combine with dissolved oxygen molecules to generate peroxide radicals. As a result, the generated reactive species e^-, h^+, $O_2^\bullet$, $^\cdot OH$, H_2O_2 react with the pollutant for further degradation [47]. The plausible mechanism of dye degradation over the surface of composite nanomaterial has been depicted in Fig. 10.

Eqs. (8)–(12) are the probable reactions for excitation and dye removal mechanisms. $LaSb + h\nu \rightarrow LaSb\ (e^-_{CB} + h^+_{VB})$ (8)

$2H^+ + e^-_{CB} + O_2 \rightarrow H_2O_2$ (9)

$H_2O_2 + h^+ \rightarrow \bullet OOH + H^+$ (10)

$H_2O + \bullet OOH \rightarrow \bullet OH + H_2O + O_2$ (11)

Reactive species ($\bullet OH$, h^+/ H_2O_2/e^-) + Dye (organic pollutant)→ Degradation products (12)

3.7.2. Role of reactive species

During the photodegradation reactions, various reactive oxygen species (e^-, h^+, $O_2^\bullet$, $^\bullet OH$, H_2O_2) are generated, which play a crucial role in the degradation of organic dyes and pollutants [52]. To investigate the mechanism of photodegradation and to determine the dominant role of reactive species in the degradation pathway, scavenging experiments are been carried out. In scavenging experiments, various scavengers are used and their effect was elucidated in terms of a decrease in the first-order rate constant. The scavengers like isopropyl alcohol (IPA), benzoquinone (BZ), sodium nitrate (SN), and ammonium oxalate (AO) were added to the reaction mixture to quench different reactive and the corresponding effect was examined in terms of a decrease in the rate constant. As shown in Fig. 11a, the addition of scavengers had a pronounced effect on photodegradation and had shown a decrease in the first-order rate constant [53]. The decrease in rate constant was maximum for IPA followed by BZ, SN, and AO. These results depicted the involvement of all reactive species in the photodegradation process but the major species were found to be hydroxyl radicals ($^\bullet OH$).

3.7.3. Recycling experiments

For a good catalyst, the first and foremost requirement is its recyclability and long-term storage. In our case, this property was checked by carrying out recycling experiments. The recycling experiments were carried out in the same manner as photocatalytic reactions carried above and after each cycle, the catalyst was recovered through filtration, followed by centrifugion and was dried and used in another cycle. The same process was continued up to four consecutive cycles. It was observed from Fig. 11b, that the catalytic activity was not much decreased and was maintained at 86% after four recycling runs. The slight decrease in the catalytic activity of the $LaFe_2O_3/Sb_2O_3$ nanocomposite after four runs may be due to the errors in retrieving the ctatlyst or weight loss during the recovery. Thus, recycling experiments demonstrated the recyclability and long-term storage of the prepared nanocomposite.

4. Conclusion

In summary, the hydrothermal method successfully synthesized a binary nanocomposite and utilized as a photocatalyst for the photodegradation of malachite green dye under visible light. The photocatalytic results demonstrate good redox behaviour and efficient charge transfer kinetics across the heterojunction interface. The lower charge transfer resistance and higher surface area of binary nanocomposite have resulted in efficient degradation of organic dye in a short period. The mechanistic details suggest major involvement of hydroxyl radicals in the degradation pathway. The catalyst was seen to be recyclable with almost the same efficiency after various recycling cycles.

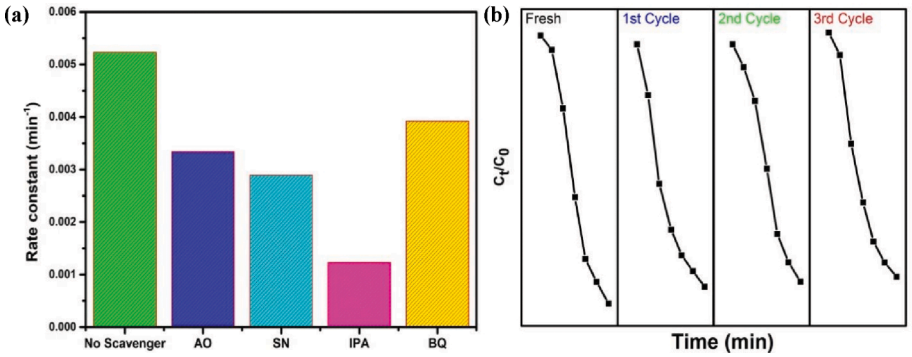

Fig. 11. (a) Scavenging experiments for elucidation of degradation mechanism. (b) Recycling experiments to check the reliability and durability of the catalyst.

Declaration of Competing Interest

The authors declare that they have no known competing financial interests or personal relationships that could have appeared to influence the work reported in this paper.

Data availability

No data was used for the research described in the article.

Acknowledgments

The authors are thankful to Prof. Abdul Rahman Khan, Head, Department of Chemistry, Integral University, Lucknow, and Prof. Anil Mishra, Head, Department of Chemistry, University of Lucknow. They are also thankful to the R & D cell of Integral University for providing the Manuscript Communication Number (IU/R&D/2023-MCN0001811). The authors also acknowledge the Department of Chemistry, University of Lucknow for providing the necessary requisite laboratory facilities and the USIF, Aligarh Muslim University, Aligarh for providing analytical and microscopic facilities.

References

[1] A.S. Ganie, S. Bano, N. Khan, S. Sultana, Z. Rehman, M.M. Rahman, S. Sabir, F. Coulon, M.Z. Khan, Nanoremediation technologies for sustainable remediation of contaminated environments: Recent advances and challenges, Chemosphere 275 (2021), 130065, https://doi.org/10.1016/j.chemosphere.2021.130065.

[2] A. Shafi, N. Ahmad, S. Sultana, S. Sabir, M.Z. Khan, Ag_2S-sensitized NiO-ZnO heterostructures with enhanced visible light photocatalytic activity and acetone sensing property, ACS Omega 4 (2019) 12905–12918, https://doi.org/10.1021/acsomega.9b01261.

[3] S. Ullah, A.U. Rahman, F. Ullah, A. Rashid, T. Arshad, E. Viglašová, M. Galamboš, N.M. Mahmoodi, H. Ullah, Adsorption of malachite green dye onto mesoporous natural inorganic clays: their equilibrium isotherm and kinetics studies, Water 13 (13) (2021) 965, https://doi.org/10.3390/W13070965.

[4] S. Jabeen, N. Ahmad, S. Bala, D. Bano, T. Khan, Nanotechnology in environmental sustainability and performance of nanomaterials in recalcitrant removal from contaminated Water: a review, Int J Nano Dimens 14 (1) (2023) 1–28, https://doi.org/10.22034/IJND.2022.1963262.2162.

[5] I. Corsi, M. Winther-Nielsen, R. Sethi, C. Punta, C. Della Torre, G. Libralato, G. Lofrano, L. Sabatini, M. Aiello, L. Fiordi, F. Cinuzzi, A. Caneschi, D. Pellegrini, I. Buttino, Ecofriendly nanotechnologies and nanomaterials for environmental applications: Key issue and consensus recommendations for sustainable and ecosafe nanoremediation, Ecotoxicol Environ Saf. 154 (2018) 237–244, https://doi.org/10.1016/j.ecoenv.2018.02.037.

[6] M. Grassi, G. Kaykioglu, V. Belgiorno, G. Lofrano, Removal of Emerging Contaminants from Water and Wastewater by Adsorption Process, in: Springer, Dordrecht, 2012, 15–37. doi:10.1007/978-94-007-3916-1_2.

[7] E.L. Gregoraszczuk, A. Ptak, Endocrine-disrupting chemicals: some actions of POPs on female reproduction, Int. J. Endocrinol. 2013 (2013), https://doi.org/10.1155/2013/828532.

[8] B.S. Rubin, Bisphenol A: an endocrine disruptor with widespread exposure and multiple effects, J. Steroid Biochem. Mol. Biol. 127 (2011) 27–34, https://doi.org/10.1016/J.JSBMB.2011.05.002.

[9] F. Amalina, A.S. Abd Razak, S. Krishnan, A.W. Zularisam, M. Nasrullah, A review of eco-sustainable techniques for the removal of Rhodamine B dye utilizing biomass residue adsorbents, Phys. Chem. Earth 128 (2022), https://doi.org/10.1016/J.PCE.2022.103267.

[10] R. Bushra, S. Mohamad, Y. Alias, Y. Jin, M. Ahmad, Current approaches and methodologies to explore the perceptive adsorption mechanism of dyes on low-cost agricultural waste: a review, Micropor. Mesopor. Mater. 319 (2021), 111040, https://doi.org/10.1016/J.MICROMESO.2021.111040.

[11] M. Ismael, Environmental remediation and sustainable energy generation via photocatalytic technology using rare earth metals modified g-C_3N_4: a review, J. Alloys Comps. 167469 (2022), https://doi.org/10.1016/j.jallcom.2022.167469.

[12] M. Ismael, Structure, properties, and characterization of mullite-type materials $Bi_2M_4O_9$ and their applications in photocatalysis: a review, J. Environ. Chem. Eng. 108640 (2022), https://doi.org/10.1016/j.jece.2022.108640.

[13] M. Ismael, Latest progress on the key operating parameters affecting the photocatalytic activity of TiO_2-based photocatalysts for hydrogen fuel production: a comprehensive review, Fuel 303 (2021), 121207, https://doi.org/10.1016/j.fuel.2021.121207.

[14] I. Khan, K. Saeed, I. Khan, Nanoparticles: Properties, applications and toxicities, Arab. J. Chem. 12 (2019) 908–931, https://doi.org/10.1016/j.arabjc.2017.05.011.

[15] M.M. Khan, S.F. Adil, A. Al-Mayouf, Metal oxides as photocatalysts, J. Saudi Chem. Soc. 19 (2015) 462–464, https://doi.org/10.1016/j.jscs.2015.04.003.

[16] P.S. Sardar, S. Ghosh, M. Biswas, N. Ballav, Highly conductive poly furan-13X zeolite-polyaniline composite, Polym. J. 40 (2008) 1199–1203, https://doi.org/10.1295/polymj.PJ2008172.

[17] M. Ismael, Y. Wu, A facile synthesis method for fabrication of $LaFeO_3$/gC_3 N_4 nanocomposite as efficient visible-light-driven photocatalyst for photodegradation of RhB and 4-CP, New J. Chem. 43 (35) (2019) 13783–13793.

[18] M. Ismael, M. Wark, Perovskite-type $LaFeO_3$: photoelectrochemical properties and photocatalytic degradation of organic pollutants under visible light irradiation, Catal. 9 (2019) 342, https://doi.org/10.3390/CATAL9040342.

[19] M. Ismael, Ferrites as solar photocatalytic materials and their activities in solar energy conversion and environmental protection: a review, Sol. Energy Mater. Sol. Cells 219 (2021), 110786, https://doi.org/10.1016/j.solmat.2020.110786.

[20] S. Bano, A.S. Ganie, S. Sultana, M.Z. Khan, S. Sabir, The non-enzymatic electrochemical detection of glucose and ammonia using ternary biopolymer based-nanocomposites, New J. Chem. 45 (2021) 8008–8021, https://doi.org/10.1039/D1NJ00474C.

[21] P. Aranda, M. Darder, R. Fernández-Saavedra, M. Ló Pez-Blanco, E. Ruiz-Hitzky, Relevance of polymer-and biopolymer-clay nanocomposites in electrochemical and electroanalytical applications, (2005). doi:10.1016/j.tsf.2005.08.284.

[22] F. Haque, T. Daeneke, K. Kalantar-zadeh, J.Z. Ou, Two-dimensional transition metal oxide, and chalcogenide-based photocatalysts, Nano-Micro Lett. 10 (2018), https://doi.org/10.1007/S40820-017-0176-Y.

[23] M. Li, L. Zhu, X. Liu, Y. Yu, H. Zhang, B. Yu, J. Zheng, N. Zhang, C. Yu, B.H. Chen, Synthesis of antimony trioxide crystals with various morphologies and their UV-Vis-NIR reflectance performance, ChemistrySelect. 3 (2018) 4310–4314, https://doi.org/10.1002/SLCT.201800077.

[24] A.K. Jha, K. Prasad, K. Prasad, Biosynthesis of Sb_2O_3 nanoparticles: a low-cost green approach, Biotechnol J. 4 (2009) 1582–1585, https://doi.org/10.1002/BIOT.200900144.

[25] B.M. Pirzada, R.K. Pushpendra, B.S. Kunchala Naidu, Synthesis of $LaFeO_3$/Ag_2CO_3 Nanocomposites for photocatalytic degradation of rhodamine B and p-chlorophenol under natural sunlight, ACS Omega 4 (2019) 2618–2629, https://doi.org/10.1021/ACSOMEGA.8B02829/ASSET/IMAGES/MEDIUM/AO-2018-028299_M006.GIF.

[26] M. Humayun, H. Ullah, M. Usman, A. Habibi-Yangjeh, A.A. Tahir, C. Wang, W. Luo, Perovskite-type lanthanum ferrite based photocatalysts: preparation, properties, and applications, J. Energy Chem. 66 (2022) 314–338, https://doi.org/10.1016/j.jechem.2021.08.023.

[27] M.A.P. Yazdi, L. Lizarraga, P. Vernoux, A. Billard, P. Briois, Catalytic properties of double substituted lanthanum cobaltite nanostructured coatings prepared by reactive magnetron sputtering, Catal 9 (9) (2019) 381, https://doi.org/10.3390/CATAL9040381.

[28] A.R. Indurkar, V.D. Sangoi, N.D. Moon, M.S. Nimbalkar, Novel synthesis of ultra-fine Sb2 O3 nanocubes using plant extract, IET Nanobiotechnol. 13 (2019) 593–596, https://doi.org/10.1049/IET-NBT.2018.5314.

[29] M. Amiri, M. Salavati-Niasari, A. Akbari, T. Gholami, Removal of malachite green (a toxic dye) from water by cobalt ferrite silica magnetic nanocomposite: herbal and green sol-gel autocombustion synthesis, Int. J. Hydrogen Energy 42 (39) (2017) 24846–24860, https://doi.org/10.1016/j.ijhydene.2017.08.077.

[30] P. Sukpanish, B. Lertpanyapornchai, T. Yokoi, C. Ngamcharussrivichai, Lanthanum-doped mesostructured strontium titanates synthesized via sol–gel combustion route using citric acid as complexing agent, Mater. Chem. Phys. 181 (2016) 422–431, https://doi.org/10.1016/J.MATCHEMPHYS.2016.06.078.

[31] A.S. Ganie, S. Bano, S. Sultana, S. Sabir, M.Z. Khan, Ferrite nanocomposite based electrochemical sensor: characterization, voltammetric and amperometric studies for electrocatalytic detection of formaldehyde in aqueous media, Electroanalysis (2021), https://doi.org/10.1002/elan.202060179.

[32] X. Wei, T. Xie, L. Peng, W. Fu, J. Chen, Q. Gao, G. Hong, D. Wang, Effect of heterojunction on the behavior of photogenerated charges in Fe_3O_4@Fe_2O_3 nanoparticle photocatalysts, J. Phys. Chem. C. 115 (2011) 8637–8642, https://doi.org/10.1021/JP111250Z/ASSET/IMAGES/MEDIUM/JP-2010-11250Z_0005.GIF.

[33] J. Zia, M. Rashad, U. Riaz, Photocatalytic degradation of anti-inflammatory drug using POPD/Sb2O3 organic-inorganic nanohybrid under solar light, J. Mater. Res. Technol. 8 (2019) 4079–4093, https://doi.org/10.1016/J.JMRT.2019.07.017.

[34] T. Mohapatra, P.K. Chaudhari, P. Ghosh, Photo-Assisted Fenton Decomposition of Organic Contaminants Under Visible-Light Illumination. In Removal of Refractory Pollutants from Wastewater Treatment Plants, CRC Press, 2021, pp. 389–398.

[35] Y. Akinay, H.C. Kazici, I.N. Akkuş, F. Salman, Synthesis of 3D Sn doped Sb_2O_3 catalysts with different morphologies and their effects on the electrocatalytic hydrogen evolution reaction in acidic medium, Ceram. Int. 47 (20) (2021) 29515–29524, https://doi.org/10.1016/j.ceramint.2021.07.278.

[36] J. Xu, C. Xu, L. Niu, C. Kang, Surface modification of Sb_2O_3 nanoparticles with dioctylphthalate, Appl. Surf. Sci. 485 (2019) 35–40, https://doi.org/10.1016/j.apsusc.2019.04.007.

[37] M. Saquib, A. Halder, Ensemble effect of Ni in bimetallic PtNi on reduced graphene oxide support for temperature-dependent formic acid oxidation, ChemistrySelect. 3 (2018) 3909–3917, https://doi.org/10.1002/slct.201800268.

[38] N. Ahmad, S. Sultana, A. Azam, S. Sabir, M.Z. Khan, Novel bio-nanocomposite materials for enhanced biodegradability and photocatalytic activity, New J. Chem. 41 (2017) 10198–10207, https://doi.org/10.1039/c7nj00842b.

[39] L. Sharma, H.S. Khushwaha, A. Mathur, A. Halder, Role of molybdenum in Ni-MoO_2 catalysts supported on reduced graphene oxide for temperature dependent hydrogen evolution reaction, J. Solid State Chem. 265 (2018) 208–217, https://doi.org/10.1016/j.jssc.2018.06.005.

[40] L. Sharma, T. Botari, C.S. Tiwary, A. Halder, Hydrogen evolution at the in situ MoO_3/MoS_2 heterojunctions created by nonthermal O_2 plasma treatment, ACS

Appl. Energy Mater. 3 (2020) 5333–5342, https://doi.org/10.1021/acsaem.0c00369.
[41] N. Ahmad, S. Sultana, G. Kumar, M. Zuhaib, S. Sabir, M.Z. Khan, Polyaniline based hybrid bionanocomposites with enhanced visible light photocatalytic activity and antifungal activity, J. Environ. Chem. Eng. 7 (2019), 102804, https://doi.org/10.1016/J.JECE.2018.11.048.
[42] S. Sultana, M.Z. Rafiuddin, K. Khan, A.S. Umar, M. Ahmed, Shahadat, SnO_2-SrO based nanocomposites and their photocatalytic activity for the treatment of organic pollutants, J. Mol. Struct. 1098 (2015) 393–399, https://doi.org/10.1016/j.molstruc.2015.06.032.
[43] O. Mehraj, B.M. Pirzada, N.A. Mir, S. Sultana, S. Sabir, Ag $_2$ S sensitized mesoporous Bi $_2$ WO_6 architectures with enhanced visible light photocatalytic activity and recycling properties, RSC Adv. 5 (2015) 42910–42921, https://doi.org/10.1039/C5RA05117G.
[44] B.M. Pirzada, N.A. Mir, N. Qutub, O. Mehraj, S. Sabir, M. Muneer, Synthesis, characterization and optimization of photocatalytic activity of TiO_2/ZrO_2 nanocomposite heterostructures, Mater. Sci. Eng. B Solid-State Mater. Adv. Technol. 193 (2015) 137–145, https://doi.org/10.1016/j.mseb.2014.12.005.
[45] B.M. Pirzada, O. Mehraj, N.A. Mir, M.Z. Khan, S. Sabir, Efficient visible light photocatalytic activity and enhanced stability of BiOBr/$Cd(OH)_2$ heterostructures, New J. Chem. 39 (2015) 7153–7163, https://doi.org/10.1039/c5nj00839e.
[46] T. Sun, C. Li, Y. Bao, J. Fan, E. Liu, S-scheme $MnCo_2S_4$/g-C_3N_4 heterojunction photocatalyst for H_2 production, Acta Phys. Chim. Sin. 39 (2023) 2212009, https://doi.org/10.3866/PKU.WHXB202212009.
[47] W. Xue, H. Sun, X. Hu, X. Bai, J. Fan, E. Liu. UV-VIS-NIR-induced extraordinary H2 evolution over $W_{18}O_{49}$/Cd0. 5Zn0.5S: surface plasmon effect coupled with S-scheme charge transfer, Chin. J. Catal. 43 (2022) 234–245. doi:10.1016/S1872-2067(20)63783-4.
[48] M. Asilturk, F. Sayilkan, E. Arpac, Effect of Fe3+ion doping to TiO_2 on the photocatalytic degradation ofMalachite Green dye under UV and vis-irradiation, J. Photochem. Photob. A: Chem. 203 (2009) (2009) 64–71, https://doi.org/10.1016/j.jphotochem.2008.12.021.
[49] N. Zada, I. Khan, K. Saeed, Synthesis of multiwalled carbon nanotubes supported manganese and cobalt zinc oxides nanoparticles for the photodegradation of malachite green, Sep. Sci. Tech. 52 (2017) 1477–1485, https://doi.org/10.1080/01496395.2017.1285920.
[50] E.M. Mostafa, E. Amdeha, Enhanced photocatalytic degradation of malachite green dye by highly stable visible-light responsive Fe-based tri-composite photocatalysts, Environ. Sci. Pollut. Res. 29 (2022) 69861–69874, https://doi.org/10.1007/s11356-022-20745-6.
[51] N. Arsalani, S. Bazazi, M. Abuali, S. Jodeyri, A new method for preparing ZnO/CNT nanocomposites with enhanced photocatalytic degradation of malachite green under visible light, J. Photochem. Photobiol. A Chem. 389, 112207. doi.org/10.1016/j.jphotochem.2019.112207.
[52] A.M. Saad, M.R. Abukhadra, S. Abdel-Kader Ahmed, et al., Photocatalytic degradation of malachite green dye using chitosan supported ZnO and Ce–ZnO nano-flowers under visible light, J. Environ. Manage. 258 (2020) (2020), 110043, https://doi.org/10.1016/j.jenvman.2019.110043.
[53] O. Mehraj, B.M. Pirzada, N.A. Mir, M.Z. Khan, S. Sabir, A highly efficient visible-light-driven novel p-n junction Fe_2O_3 /BiOI photocatalyst: surface decoration of BiOI nanosheets with Fe_2O_3 nanoparticles, Appl. Surf. Sci. 387 (2016) 642–651, https://doi.org/10.1016/j.apsusc.2016.06.166.